





Direct imaging of long-range ferromagnetic and antiferromagnetic order in a dipolar metamaterialEinar Digernes ^{1,*}, Sam D. Sløetjes,^{1,2} Anders Strømberg ¹, Ambjørn D. Bang,¹ Fredrik K. Olsen,¹ Elke Arenholz,^{2,3} Rajesh V. Chopdekar ², Jostein K. Grepstad,¹ and Erik Folven ¹¹*Department of Electronic Systems, Norwegian University of Science and Technology, NO-7491 Trondheim, Norway*²*Advanced Light Source, Lawrence Berkeley National Laboratories, Berkeley, California 94720, USA*³*Cornell High Energy Synchrotron Source, Cornell University, Ithaca, New York 14853, USA*

(Received 6 June 2019; revised manuscript received 5 November 2019; accepted 10 January 2020; published 27 February 2020)

Magnetic metamaterials such as artificial spin ice offer a route to tailor magnetic properties. Such materials can be fabricated by lithographically defining arrays of nanoscale magnetic islands. The magnetostatic interactions between the elements are influenced by their shape and geometric arrangement and can lead to long-range ordering. We demonstrate how the magnetic order in a two-dimensional periodic array of circular disks is controlled by the lattice symmetry. Antiferromagnetic and ferromagnetic order extending through the entire array is observed for the square and hexagonal lattice, respectively. Furthermore, we show that a minute deviation from perfect circularity of the elements along a preferred direction results in room-temperature blocking and favors collinear spin textures.

DOI: [10.1103/PhysRevResearch.2.013222](https://doi.org/10.1103/PhysRevResearch.2.013222)**I. INTRODUCTION**

Luttinger and Tisza predicted that the magnetic order in a lattice of point dipoles is governed by the symmetry of the dipole lattice [1], suggesting a novel mechanism for ferromagnetic (FM) order not based on exchange interactions. However, in an atomic crystal lattice, the magnetostatic interaction between individual atoms is relatively weak and results in Curie temperatures in the sub-100-mK regime [2].

Monodomain nanomagnets can serve as a mesoscale analog to atomic magnetic moments, and they are used extensively in the study of frustration in artificial spin ice [3], emergent magnetic monopoles [4,5], and dipolar magnetic order [6–8]. Magnetic elements below a critical size will be in a monodomain state, and the magnetization of each element can be described in terms of a single macrospin [9,10]. The ground-state ordering of these macrospins is determined by the geometric arrangement of the elements [11] as well as their shape.

To first order, the total magnetization of a monodomain disk can be approximated as a point dipole. The ground-state configuration in a lattice of such dipoles is well established and is predicted to be FM for a hexagonal lattice [12,13]. Collective ferromagnetic ordering has been shown in assemblies of close-packed monodisperse nanoparticles [14–16]. For a square lattice, the predicted ground state is twofold-degenerate, with stripe-ordered antiferromagnetic

(AF) [Fig. 1(f)] and microvortex (MV) order [Fig. 1(g)] equal in energy. However, models including higher-order moments [17] or spin-wave stiffness [18] show that this degeneracy is lifted and favor AF order. Recent experiments for a square lattice were found to support the presence of long-range order, consistent with this theoretically predicted behavior [7,19].

Here, we directly image emergent long-range magnetic order in arrays of magnetostatically coupled nanoscale permalloy (Py; Ni₈₁Fe₁₉) disks arranged in square and hexagonal lattices. Depending on the lattice symmetry, FM or AF order is stabilized. We also investigate magnetization reversal of these lattices in an applied field, as well as thermal relaxation of the magnetization in the square lattice. To this end, we use soft-x-ray magnetic circular dichroism photoemission electron microscopy (XMCD-PEEM). This synchrotron-based technique with sub-100-nm spatial resolution relies on magnetic dichroism in the x-ray absorption to provide magnetic contrast.

II. EXPERIMENTAL METHODS

The dipolar metamaterials were defined in 15 nm thin films of Py coated with a 2 nm aluminum oxidation barrier, using electron beam lithography and liftoff. Metallization was done with electron beam evaporation on a silicon wafer. The patterned arrays were 20 μm × 20 μm with disks of 100 nm diam and 130 nm pitch.

Scanning electron micrographs of these arrays, displayed in Figs. 1(a) and 1(b), show that the disks are well-defined. Their physical separation ensures no exchange coupling between the disks. Image analysis of the scanning electron micrographs reveals an average elliptic distortion (ratio of major to minor axis) $\epsilon = 1.05$ with a preferred orientation of the major axis inclined 20° with the horizontal. For details, see Appendix A. We attribute this minor elliptic distortion to imperfections in the electron beam patterning process.

*einar.digernes@ntnu.no

Published by the American Physical Society under the terms of the [Creative Commons Attribution 4.0 International](https://creativecommons.org/licenses/by/4.0/) license. Further distribution of this work must maintain attribution to the author(s) and the published article's title, journal citation, and DOI.

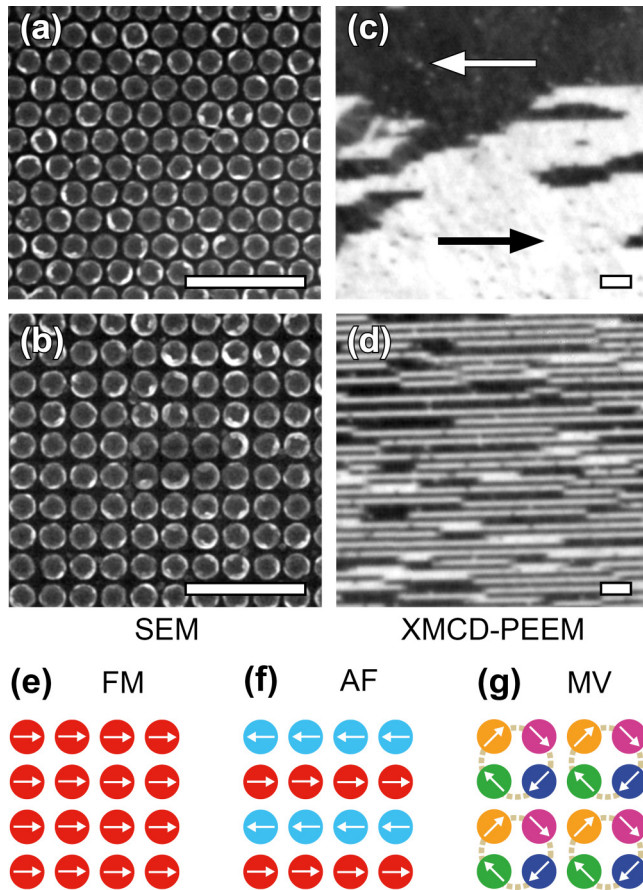


FIG. 1. Scanning electron micrographs of magnetic metamaterials composed of 100-nm-diam and 15-nm-thick disks of Py. The disks are organized in (a) hexagonal and (b) square lattices with a pitch of 130 nm and an overall size of $20 \times 20 \mu\text{m}^2$. Magnetic contrast images recorded using XMCD-PEEM reveal (c) FM order for the hexagonal lattice and (d) AF order for the square lattice. Magnetization directions are indicated by the arrows in (c). The scale bars are 500 nm. (e)–(g) FM, AF, and MV spin configurations for a square lattice.

XMCD-PEEM imaging was carried out using the PEEM-3 microscope [20] at the Advanced Light Source. Magnetization maps were obtained as the difference between two PEEM images recorded with right-handed and left-handed circular polarized x rays with a photon energy of 707 eV, corresponding

to the Fe L_3 absorption edge. Regions magnetized parallel and antiparallel to the incident x rays provide maximum difference in contrast and thus appear as black/white in the XMCD-PEEM micrographs. Regions magnetized perpendicular to the incident x rays appear gray.

III. RESULTS AND DISCUSSION

The XMCD-PEEM images reveal FM ordering in the hexagonal lattice [Fig. 1(c)] and AF ordering in the square lattice [Fig. 1(d)]. The results demonstrate that magnetostatic coupling supports long-range order in these magnetic metamaterials. Furthermore, the magnetic order depends directly on the lattice geometry.

The switching behavior of these arrays was investigated by applying small in-plane magnetic field pulses *in situ*, followed by XMCD-PEEM imaging in remanence. Figure 2 shows the magnetization maps obtained for the hexagonal lattice. A magnetic field of 19 mT was applied in order to initialize the array in a saturated state. We note from Fig. 2(a) that the array remains saturated in remanence. Subsequently, magnetic fields of 2 and 6 mT were applied in the reverse direction [Figs. 2(b) and 2(c)]. We then observe array magnetization reversal via a multidomain FM state with extended domains of macrospins (several microns across) to a saturated state in the opposite direction. To maximize the magnetostatic interaction, the disks were made as large as possible while still preserving a monodomain ground state. Due to variation in size, some magnets may have entered a flux-closure configuration [9]. The speckles observed in the magnetization maps in Fig. 2 may be attributed to such flux-closure configurations. We note a predominant orientation of the domain walls in Fig. 2(b) along the same direction as the average elliptic distortion of the disks ($\sim 20^\circ$ with the horizontal).

The corresponding magnetization reversal for the square lattice is shown in Fig. 3. After initialization, this lattice is predominantly magnetized in one direction in remanence [Fig. 3(a)]. However, we note the presence of short chains of disks with opposite magnetization not seen in the hexagonal lattice. We attribute this observation to the fact that the square lattice is far from its dipolar-coupled ground state when saturated. Consequently, some macrospins reverse their direction of magnetization to locally reduce the magnetostatic energy upon removal of the external field. The observation of

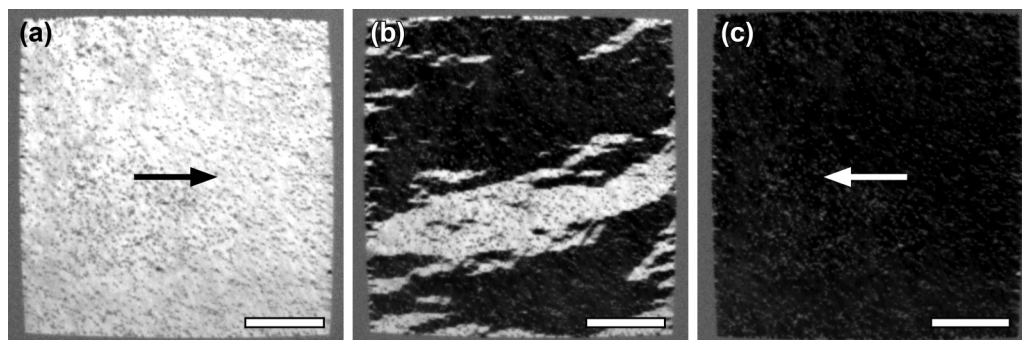


FIG. 2. Magnetization reversal for the hexagonal lattice. XMCD-PEEM magnetic contrast images with magnetization directions indicated by the arrows. The images are recorded in remanence, following in-plane magnetic field pulses (from left to right) of (a) 19 mT, (b) -2 mT, (c) and -6 mT. The scale bars are $5 \mu\text{m}$.

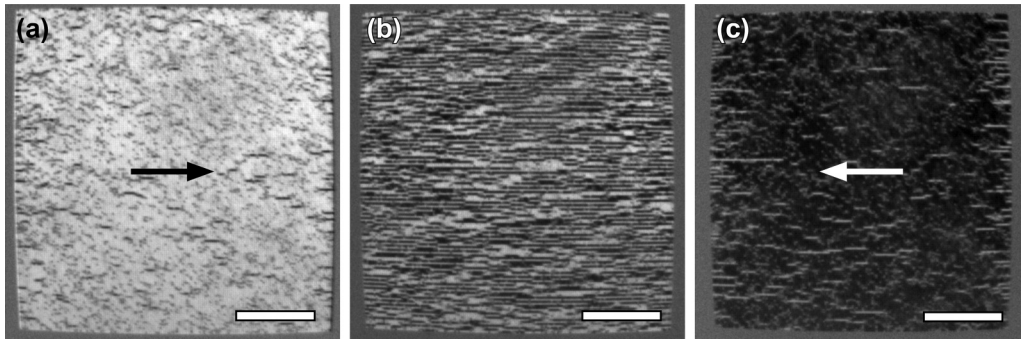


FIG. 3. Magnetization reversal for the square lattice. XMCD-PEEM magnetic contrast images with magnetization directions indicated by the arrows. The images are recorded in remanence, following in-plane magnetic-field pulses (from left to right) of (a) 19 mT, (b) -2 mT, (c) and -6 mT. The scale bars are $5 \mu\text{m}$.

a saturated state at remanence suggests that the anisotropy of the individual disks prevents relaxation of the array to its AF ground state, i.e., the system is in a blocked regime. When a small reverse field of 2 mT is applied, the array passes through a state of predominantly AF order [Fig. 3(b)], before the magnetization saturates in the opposite direction [Fig. 3(c)] at a field of 6 mT.

Since XMCD-PEEM is only sensitive to magnetization along the direction of the incident x rays, it can be argued that AF order cannot be easily distinguished from MV order. To unambiguously determine the magnetic configuration for the square lattice, we recorded XMCD-PEEM images with x rays incident at different azimuthal angles ($\phi = 0^\circ, 25^\circ, 45^\circ, 67^\circ, 90^\circ$, and 180°) to generate a complete in-plane vector magnetization map (Fig. 4). In this map, stripes of horizontal magnetization are predominant. This finding is not compatible with MV order.

Blocking was investigated further by heating the sample. At temperatures below the blocking temperature T_B , the thermal energy is insufficient to switch the individual nanomagnets. The system is then frozen in a local energy minimum rather than in its global ground state. The sample was saturated *ex situ* in a 0.3 T magnetic field. Figure 5 displays the magnetization map (a) after 2 days at room temperature and (b) after subsequent heating to 210°C for 1.5 h. We observe nucleation and growth of chains with reversed magnetization starting from the vertical edges of the array. At this point, the heater was turned off, and the sample was left to cool at an estimated rate of $5\text{--}10$ K/min. After cooling to room temperature, an AF pattern extending throughout the sample was recorded [Fig. 5(c)].

The selection of AF over MV order has been previously explained by invoking higher-order moments [17] to account for deviations from a purely dipolar field distribution due to the finite size of the disks. We have used micromagnetic modeling [21] to quantify the demagnetization energy for the FM, AF, and MV order in the square lattice; see Appendix B. For perfectly circular disks ($\epsilon = 1.00$), we find that the AF and MV spin configurations are lowest in energy. The difference in demagnetization energy between these spin textures is within the numerical accuracy of the analysis ($\ll k_B T$) and the two configurations are thus considered degenerate. Thus, the selection of AF order in our system cannot be directly attributed to a non-dipolar field distribution. However,

if disks with elliptic distortions ($\epsilon = 1.05$) are introduced, the degeneracy between AF and MV order is lifted, selecting the collinear AF ground state. We note no qualitative difference

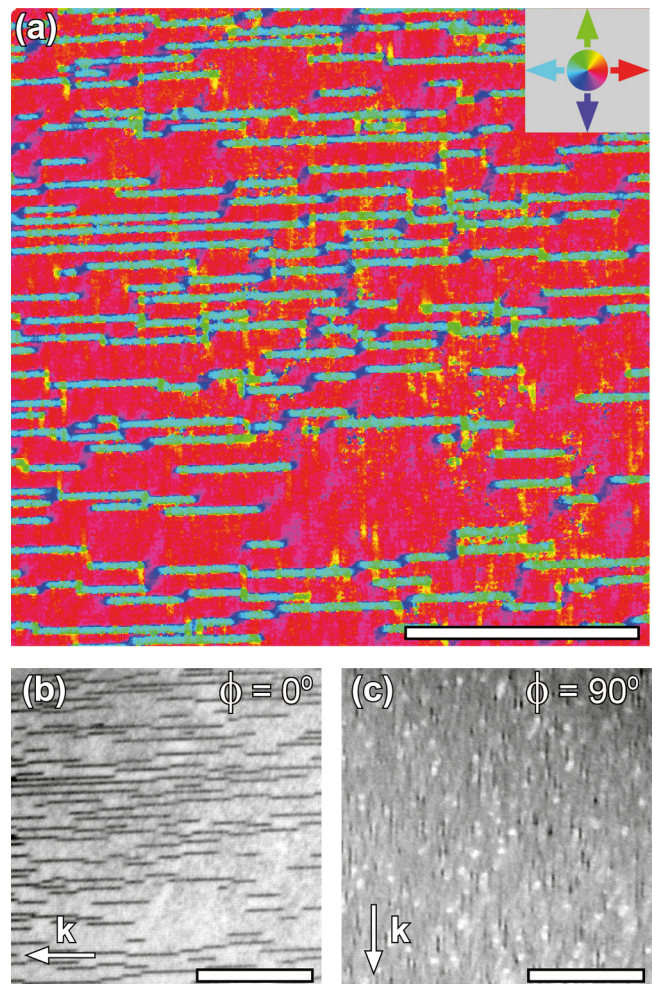


FIG. 4. Experimental in-plane vector magnetization map for the square lattice; (a) with the direction of magnetization indicated by the color wheel, (b) XMCD-PEEM micrographs with magnetic contrast along the horizontal direction ($\phi = 0^\circ$), and (c) along the vertical ($\phi = 90^\circ$) direction, as indicated by the arrows. The predominance of stripes with horizontal magnetization is compatible with AF order and not with MV order. The scale bars are $2 \mu\text{m}$.

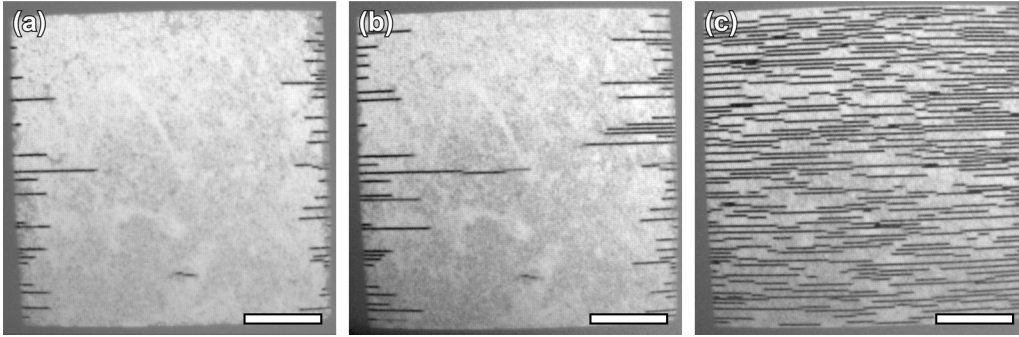


FIG. 5. Thermal relaxation for the square lattice; XMCD-PEEM magnetic contrast images measured at (a) room temperature, (b) after heating to 210 °C for 1.5 h, and (c) after passive cooling to room temperature for 12 h. The scale bars are 5 μm .

if the elliptic distortion is along 0° or 20° to the horizontal. This analysis shows that the measured elliptic distortion offers an independent mechanism for selection of the AF order.

The elliptic distortion of the disks will also affect the blocking temperature. This is briefly discussed in Appendix B. We find that the average elliptic distortion in this experiment results in an energy barrier for magnetization reversal of 3.0 eV for individual disks at room temperature. However, for disks on a square lattice the activation barrier for switching from a saturated state to AF order is considerably reduced due to dipolar coupling with the surrounding disks. For an elliptic distortion of $\epsilon = 1.05$, the barrier is reduced to 1.4 eV. This finding is in keeping with the observed thermal relaxation observed for a saturated square lattice at 210 °C (Fig. 5).

IV. CONCLUSION

In conclusion, we show by direct imaging that lattices of dipolar-coupled nanomagnets can support long-range magnetic order. This ordering depends on the lattice geometry, with hexagonal and square lattices supporting FM and AF order, respectively. We find that the magnetic ground state of the arrays is affected by the shape of the nanomagnets and note that a small directional elliptic distortion of the disk-shaped elements on a square lattice favors collinear spin arrangements. The present work may prove useful to engineering of magnetic metamaterials and stimulate further investigations of dipolar-coupled systems.

ACKNOWLEDGMENTS

This research used resources of the Advanced Light Source, which is a DOE Office of Science User Facility under Contract No. DE-AC02-05CH11231. S.D.S. acknowledges support from the ALS Doctoral Fellowship in Residence. Partial funding was obtained from the Norwegian Ph.D. Network on Nanotechnology for Microsystems, which is sponsored by the Research Council of Norway, Division for Science, under Contract No. 221860/F60. The Research Council of Norway is acknowledged for support to the Norwegian Micro- and Nanofabrication Facility, Research Council of Norway, under Contract No. 245963/F50.

APPENDIX A: SHAPE ANALYSIS

Imperfections in nanopatterns defined with electron beam lithography are inevitable. Even when the process is optimized, there will be variations between the individual structures.

In Fig. 6, ellipses are fitted to the nanodisks in the scanning electron micrographs of the square array, with a nominal disk diameter of 100 nm and a pitch of 130 nm. The scanning electron micrograph is shown as recorded in Fig. 6(a) and with the fitted ellipses in Fig. 6(b). The elliptic distortion $\epsilon = \frac{l_{\text{major}}}{l_{\text{minor}}}$ is plotted versus rotation of the major axis in Fig. 6(c). The polar histogram in the inset shows the distribution of major axis orientations. The elements have an elliptic distortion of up to $\epsilon = 1.16$, with an average of $\epsilon = 1.05$. The polar histogram reveals a preferential orientation of the major axis at 20° with respect to the horizontal. We note that this preferential orientation is systematic and possibly due to a deviation from circularity of the electron beam. These results are also representative for the hexagonal lattice.

APPENDIX B: MICROMAGNETIC MODELING

Here, the micromagnetic modeling is described in detail. We have used these models to make rough estimates of the effect of the elliptic distortion of the disks on the long-range order and blocking temperature. Typical material parameters for Py were used, with $M_{\text{sat}} = 860 \text{ kA/m}$ and a small cell size of $0.5 \times 0.5 \times 0.5 \text{ nm}^3$ to reduce the effects of projecting circles onto a discrete simulation lattice.

1. Effect of elliptic distortion on the magnetic ground state

The effect of the preferential disk ellipticity on the demagnetization energy for the FM, MV, and AF order was calculated for a unit cell of 2×2 disks with 130 nm pitch, repeated for an overall array of 154×154 disks, corresponding to the fabricated sample. The demagnetization energy per disk was calculated for arrays initialized with FM, AF, and MV order, respectively, and with uniform magnetization within each disk (Fig. 7). For perfectly circular disks, the MV and AF configurations were degenerate at room temperature with $\Delta E = E_{\text{MV}} - E_{\text{AF}} = -0.008 \text{ meV} \ll k_B T$. For an elliptic distortion of $\epsilon = 1.05$ control this, the degeneracy is lifted, with AF order being 1.8 eV lower in energy. Thus, for the square lattice simple micromagnetic analysis predicts a degenerate ground

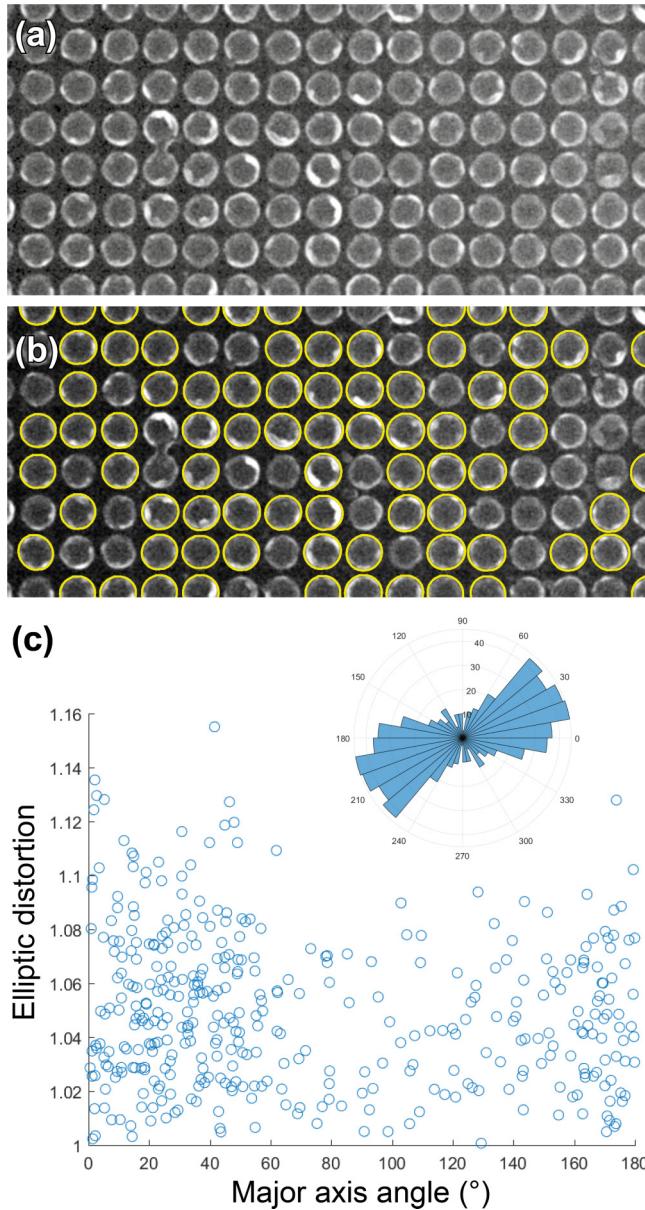


FIG. 6. Fitting ellipses to scanning electron micrographs. (a) Scanning electron micrograph of the square-lattice sample with disk diameter 100 nm and pitch 130 nm. (b) Outline of ellipses fitted to the disks. (c) Ellipticity and major axis orientation for each of the fitted ellipses. The inset shows a polar histogram for distribution of the major axis orientation.

state for perfectly circular disks. However, this degeneracy is lifted when a preferential elliptic distortion is present.

2. Single disk blocking temperature

In the following section, the effect of elliptic distortion on the shape anisotropy and blocking temperature (T_B) is estimated for single disks. Distortions up to 20% were simulated, corresponding to the range observed experimentally. The shape anisotropy was assessed from the difference in demagnetization energy between uniformly magnetized elements oriented along the major and minor axes, respectively.

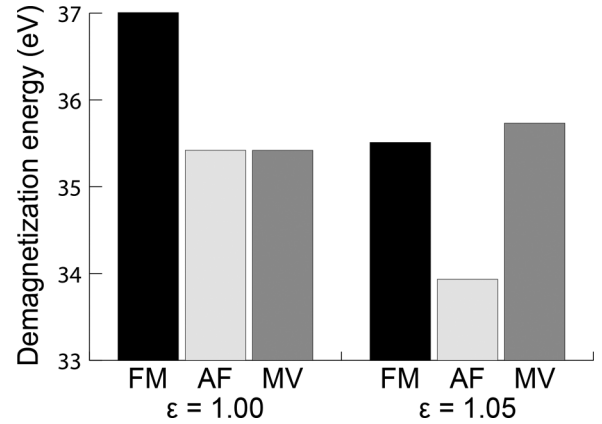


FIG. 7. Demagnetization energy per disk for perfectly circular ($\epsilon = 1.00$) and elliptically distorted ($\epsilon = 1.05$) disks obtained from micromagnetic calculations for FM, AF, and MV spin configurations on the square lattice.

For an elliptic distortion $\epsilon = 1.05$, the energy difference is $\Delta E_{\text{shape}} = 3$ eV. The Néel-Brown expression can be used to estimate the relaxation time τ for a magnet with an energy barrier ΔE ,

$$\tau = \tau_0 \exp \frac{\Delta E}{k_B T}, \tag{B1}$$

where we use $\tau_0 = 10^{-10}$ s as the inverse attempt frequency [22]. For $\Delta E = \Delta E_{\text{shape}} = 3$ eV, the relaxation time $\tau = 2.0 \times 10^{21}$ s for $T = 210^\circ\text{C}$, which implies that the magnetization of the average disk is blocked even at the highest temperature accessed in our experiment.

3. Lowering of activation barrier due to magnetostatic coupling

The magnetostatic coupling of neighboring magnets may reduce the activation energy for switching. This is the case for the square lattice when going from a saturated to an AF configuration. To keep the model simple, a system of 3×3 magnets is considered as shown in Fig. 8. The array is initially magnetized to the right, except for one disk on the right hand side of the center magnet, pointing to the left. When the center magnet is rotated 90° , the demagnetization energy is reduced by 1.6 eV.

If we assume that the energy barrier for a magnet with $\epsilon = 1.05$ is reduced from 3 to 1.4 eV by the dipolar coupling, the



FIG. 8. The demagnetization energy is reduced by 1.6 and 3.2 eV upon rotation of the center disk by 90° and 180° , respectively.

relaxation time at a temperature of 210 °C is reduced to 4.1×10^4 s. The accelerated relaxation rate observed in Fig. 5 for

the square lattice during heating is in qualitative agreement with this finding.

-
- [1] J. M. Luttinger and L. Tisza, *Phys. Rev.* **70**, 954 (1946).
- [2] M. R. Roser and L. R. Corruccini, *Phys. Rev. Lett.* **65**, 1064 (1990).
- [3] R. F. Wang *et al.*, *Nature (London)* **439**, 303 (2006).
- [4] S. Ladak, D. E. Read, G. K. Perkins, L. F. Cohen, and W. R. Branford, *Nat. Phys.* **6**, 359 (2010).
- [5] E. Mengotti, L. J. Heyderman, A. F. Rodríguez, F. Nolting, R. V. Hügli, and H. B. Braun, *Nat. Phys.* **7**, 68 (2011).
- [6] M. Ewerlin, D. Demirbas, F. Brüßing, O. Petracic, A. A. Ünal, S. Valencia, F. Kronast, and H. Zabel, *Phys. Rev. Lett.* **110**, 177209 (2013).
- [7] N. Leo *et al.*, *Nat. Commun.* **9**, 2850 (2018).
- [8] D. Louis, D. Lacour, M. Hehn, V. Lomakin, T. Hauet, and F. Montaigne, *Nature Mater.* **17**, 1076 (2018).
- [9] R. P. Cowburn, D. K. Koltsov, A. O. Adeyeye, M. E. Welland, and D. M. Tricker, *Phys. Rev. Lett.* **83**, 1042 (1999).
- [10] S. Bedanta and W. Kleemann, *J. Phys. D* **42**, 013001 (2009).
- [11] S. D. Sløtjes, H. H. Urdahl, J. K. Grepstad, and E. Folven, *AIP Adv.* **7**, 056325 (2017).
- [12] V. M. Rozenbaum, *Sov. Phys. Usp.* **34**, 883 (1991).
- [13] P. Politi and M. G. Pini, *Phys. Rev. B* **66**, 214414 (2002).
- [14] S. Bedanta, T. Eimüller, W. Kleemann, J. Rhensius, F. Stromberg, E. Amaladass, S. Cardoso, and P. P. Freitas, *Phys. Rev. Lett.* **98**, 176601 (2007).
- [15] K. Yamamoto, C. R. Hogg, S. Yamamuro, T. Hirayama, and S. A. Majetich, *Appl. Phys. Lett.* **98**, 072509 (2011).
- [16] M. Varón, M. Beleggia, T. Kasama, R. J. Harrison, R. E. Dunin-Borkowski, V. F. Puentes, and C. Frandsen, *Sci. Rep.* **3**, 1234 (2013).
- [17] E. Y. Vedmedenko, N. Mikuszeit, H. P. Oepen, and R. Wiesendanger, *Phys. Rev. Lett.* **95**, 207202 (2005).
- [18] S. Prakash and C. L. Henley, *Phys. Rev. B* **42**, 6574 (1990).
- [19] R. Streubel, N. Kent, S. Dhuey, A. Scholl, S. Kevan, and P. Fischer, *Nano Lett.* **18**, 7428 (2018).
- [20] A. Doran, M. Church, T. Miller, G. Morrison, A. T. Young, and A. Scholl, *J. Electron Spectrosc. Relat. Phenom.* **185**, 340 (2012).
- [21] A. Vansteenkiste, J. Leliaert, M. Dvornik, M. Helsen, F. G.-. Sanchez, and B. V. Waeyenberge, *AIP Adv.* **4**, 107133 (2014).
- [22] W. F. Brown, *Phys. Rev.* **130**, 1677 (1963).